Constraints on mechanisms for the growth of gully alcoves in Gasa crater, Mars, from two-dimensional stability assessments of rock slopes

Chris H. Okubo [a,*], Livio L. Tornabene [b], Nina L. Lanza [c]

[a] Astrogeology Science Center, U.S. Geological Survey, Flagstaff, AZ 86001, United States
[b] Lunar and Planetary Laboratory, University of Arizona, Tucson, AZ 85721, United States
[c] Institute of Meteoritics, University of New Mexico, Albuquerque, NM 87131, United States

ARTICLE INFO

ABSTRACT

The value of slope stability analyses for gaining insight into the geologic conditions that would facilitate the growth of gully alcoves on Mars is demonstrated in Gasa crater. Two-dimensional limit equilibrium methods are used in conjunction with high-resolution topography derived from stereo High Resolution Imaging Science Experiment (HiRISE) imagery. These analyses reveal three conditions that may produce observed alcove morphologies through slope failure: (1) a ca. >10 m thick surface layer that is either saturated with H_2O ground ice or contains no groundwater/ice at all, above a zone of melting H_2O ice or groundwater and under dynamic loading (i.e., seismicity), (2) a 1–10 m thick surface layer that is saturated with either melting H_2O ice or groundwater and under dynamic loading, or (3) a >100 m thick surface layer that is saturated with either melting H_2O ice or groundwater and under static loading. This finding of three plausible scenarios for slope failure demonstrates how the triggering mechanisms and characteristics of future alcove growth would be affected by prevailing environmental conditions. HiRISE images also reveal normal faults and other fractures tangential to the crowns of some gully alcoves that are interpreted to be the result of slope instability, which may facilitate future slope movement. Stability analyses show that the most failure-prone slopes in this area are found in alcoves that are adjacent to crown fractures. Accordingly, crown fractures appear to be a useful indicator of those alcoves that should be monitored for future landslide activity.

Published by Elsevier Inc.

1. Introduction

Much debate is ongoing regarding the role and necessity of liquid water in the formation of martian gullies. A substantial collection of work argues that gully formation occurs under wet conditions (e.g., Malin and Edgett, 2000; Heldmann and Mellon, 2004; Balme et al., 2006; Heldmann et al., 2007; Head et al., 2008; Lanza et al., 2010; and many others), while other works discuss alternative processes of gully formation that do not require the presence of water (e.g., Treiman, 2003; Shinbrot et al., 2004; Bart, 2007; Hugenholtz, 2008). An equally contentious issue is the origin of any such liquid water, which may come from sources including melting snow or frost (e.g., Hecht, 2002; Christensen, 2003; Bridges and Lackner, 2006; Dickson et al., 2007; Levy et al., 2009), melting ground ice (e.g., Costard et al., 2002; Gilmore and Phillips, 2002; Balme et al., 2006), and geothermally-heated aquifers (e.g., Gaidos, 2001; Mellon and Phillips, 2001; Hartmann, 2001). An important caveat in this discussion is that prevailing environmental and geologic conditions may influence the

mechanism of slope failure, and thus a requirement for extant water to drive gully formation may be spatially and temporally variable (e.g., Reiss et al., 2009; Kolb et al., 2010a).

Geotechnical slope stability analysis is an important tool that deserves more widespread consideration in efforts to constrain the mechanisms that can drive the growth of gully alcoves on Mars. In this paper, the utility of slope stability analyses is demonstrated using gully alcoves in Gasa crater. We demonstrate how these analyses can shed new insight into the effects that different combinations of weathering, bedrock fracturing, seismicity, groundwater and ground ice will have on the stability these gully alcoves. Such analyses help to further characterize the types of conditions that would most effectively facilitate the formation and future growth of these alcoves through slope failure of the underlying rock mass. Throughout this paper, the term 'groundwater' refers to all subsurface water within the zone of saturation (c.f., Neuendorf et al., 2005), without restriction to a specific origin or depth.

Located in the southern equatorial region of Mars (−35.71°N, 230.72°W planetocentric), Gasa crater is sits directly within the crater-fill deposits of a larger unnamed ca. 20-km diameter crater. Gasa crater has a diameter of roughly 6.5 km and a crater retention

age of *ca.* 1.25 Ma (Schon et al., 2009). Gasa exhibits the characteristics of a youthful, fresh and well-preserved crater (Tornabene et al., 2006), providing a setting in which minimal erosion (aside from gully formation) has occurred. Gasa crater is selected for this study because the alcoves within it are well exposed, have clear exposures of bedrock, and have been imaged in high-resolution stereo and in high spectral resolution data. This paper complements other recent work in Gasa crater (Lanza et al., 2010; Kolb et al., 2010a; Conway et al., 2010) that use distinct and independent techniques for utilizing high-resolution topography to investigate potential mechanisms for gully formation.

The inner wall of Gasa crater hosts numerous hollows containing a multitude of gullies that have well-defined alcove-channel-apron morphologies (Figs. 1 and S1). Observations acquired by the High Resolution Imaging Science Experiment (HiRISE) camera shows that these gully alcoves are incised into an underlying rock mass. These HiRISE images have a pixel scale of *ca.* 0.27 m, so clasts down to a comparable diameter can be detected, and meter-scale clasts are resolved. Some areas appear smooth at the limit of HiRISE detection and are thus interpreted to consist of cobble-sized clasts and smaller. Outcrops of fractured bedrock are observed in other areas. Since Gasa crater sits within an older impact crater, impact melt and impact breccia is expected to be the dominant bedrock lithology (e.g., Grant et al., 2008; Marzo et al., 2010). The smooth-lying materials are likely composed of poorly-indurated impact breccia, colluvium or eolian sediments. Colluvium is expected from mass wasting of the interior walls of Gasa crater.

In their earlier study, Lanza et al. (2010) measure the areas and slopes of several gully alcoves in Gasa crater (Fig. 1) and elsewhere. They show that the scaling relationship between the area and slope of individual alcoves is most consistent with measurements from terrestrial gully alcoves that formed by debris flow, or saturation-induced slope failure, of slope mantling materials. Based on these results, Lanza et al. (2010) propose that a broadly-distributed near-surface groundwater source, such as ice melt, was an important condition for the formation of many of these alcoves.

Kolb et al. (2010a) measured the slopes of gully fan apices in several impact craters, including Gasa crater (Fig. 1), to better understand the conditions of gully formation. They find that the slopes of some fan apices are sufficiently shallow, less than 21°, as to indicate sediment deposition by fluidized flows. Other measured fans have steeper apices, which are consistent with emplacement by either fluidized or dry flows. Kolb et al. (2010a) suggest that some of these flows may have been fluidized by the presence of groundwater.

Recently, Conway et al. (2010) analyzed HiRISE DEMs of gullies in Gasa, plus three other southern hemisphere craters. By comparison with terrestrial gullies and hollows, the drainage morphologies of the martian gullies are found to be most consistent with formation through debris flow activity. Further, the source of the attendant water was derived predominantly from distributed surface melting instead of upwelling groundwater.

The analyses demonstrated in this paper focus on characterizing mechanisms of alcove growth that occur through landsliding of the
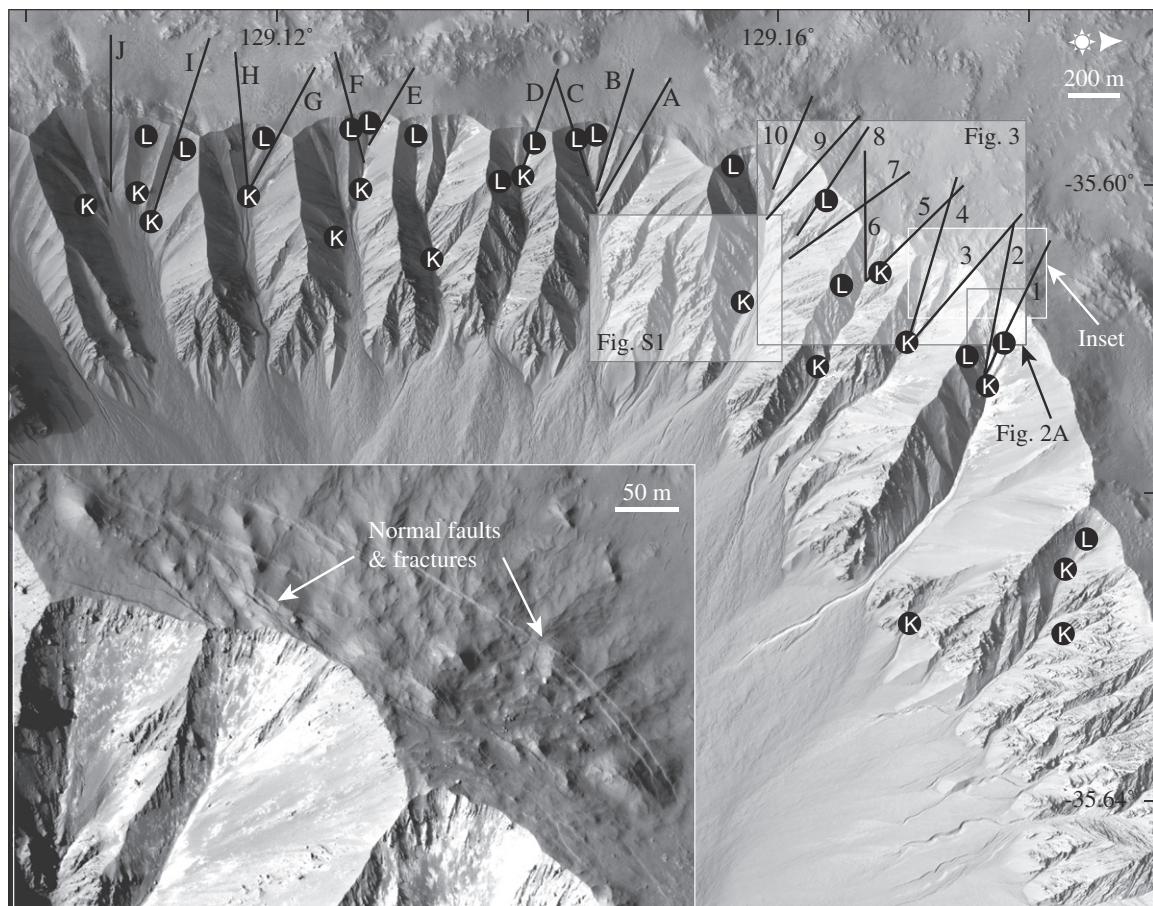

Fig. 1. Hollows containing numerous well-defined gullies along the rim of Gasa crater. Normal faults and fractures are roughly tangential to the crowns of many of the alcoves along the northeast rim of this crater (inset). Solid lines show the locations of topographic profiles analyzed in this study. Numbered profiles transect alcoves that are adjacent the crown fractures, while lettered profiles sample alcoves that are not adjacent to crown fractures. Alcoves studied by Lanza et al. (2010) are denoted with L's, and fan apices studied by Kolb et al. (2010a) are denoted with K's. Image is from HiRISE PSP_004060_1440.

underlying rock mass. Here, the rock mass is considered to be composed of materials ranging from undisturbed, in situ rock to impact breccia and colluvium, with the latter two conditions being most prevalent. This work focuses specifically on the stability of rock slopes rather than slopes composed primarily of soils and seasonal frost. Recent mass wasting events in surficial soils, or seasonal CO_2 frost (e.g., McEwen et al., 2007; Pelletier et al., 2008; Kolb et al., 2010b; Diniega et al., 2010; Dundas et al., 2010) have occurred within some gullies at Gasa crater. The stability of these younger, unconsolidated materials warrants a separate discussion and is not addressed here.

2. New insight into recent rock slope failures

HiRISE imagery of Gasa crater reveals populations of normal faults and possibly joints around the crowns of some gully alcoves (Fig. 1). The fractures generally form en echelon arrays that are roughly concentric about the adjacent alcoves. Some of these fracture arrays are also truncated where they intersect the alcove rim. Individual fracture arrays have lengths of up to several hundred meters. Based on shadow length measurements and measurements from a HiRISE digital elevation model (DEM; discussed below), the maximum apparent throws of these faults are found to be 1–2 m. The orientations of the normal faults and joints are indicative of extensional strains acting roughly orthogonal to the crowns of the alcoves.

The pattern of fracturing observed around these gully alcoves is also commonly found adjacent to the crowns of gully alcoves on Earth. This characteristic pattern of fracturing, also called "sackung" is indicative of landsliding (c.f., Varnes, 1978; Cruden and Varnes, 1996). Fracturing around the crowns of landslide alcoves can form in response to extensional strains that develop from the down-slope movement of rock (e.g. Martel, 2004). Thus the fractures observed at Gasa crater have the orientations, locations, and an extensional sense of strain, that are consistent with the normal faults and joints that develop in response to slope failure and growth of terrestrial alcoves. Based on these similarities, the fractures around the Gasa crater alcoves are inferred to have formed in a manner largely analogous to the terrestrial examples, that is, these are crown fractures that formed through processes of failure of unstable wall rock within the alcove. While the formation of these fractures during impact formation (i.e., before the gullies formed) cannot be entirely ruled out, the roughly concentric orientation of these fractures about the gully alcoves is strongly consistent with a causal relationship between the gullies and fractures. These crown fractures could also reactivate and link impact-related fracture surfaces.

The morphology of some alcove walls offers clues to the size and shape of the most recent slope failures that have occurred along them. These walls have a scalloped appearance (Fig. 2), suggestive of multiple collapses of small (10s of meters wide) and shallow-seated (a few to 10s of meters thick) wedges of rock. The volumes of rock involved in each individual shallow-seated failure would have been smaller than the size of the surrounding alcove by an order of magnitude or more. The growth of gully alcoves through smaller, incremental slope failures is common on Earth (e.g., O'Reilly et al., 2007; Ulusay et al., 2007).

3. Methods

In this study, stability analyses are employed to predict the effects that common geologic conditions would have on the tendencies and geometries of future slope failures along several existing gully alcoves in Gasa crater. The combinations of geologic conditions that both predict slope failure and most consistently
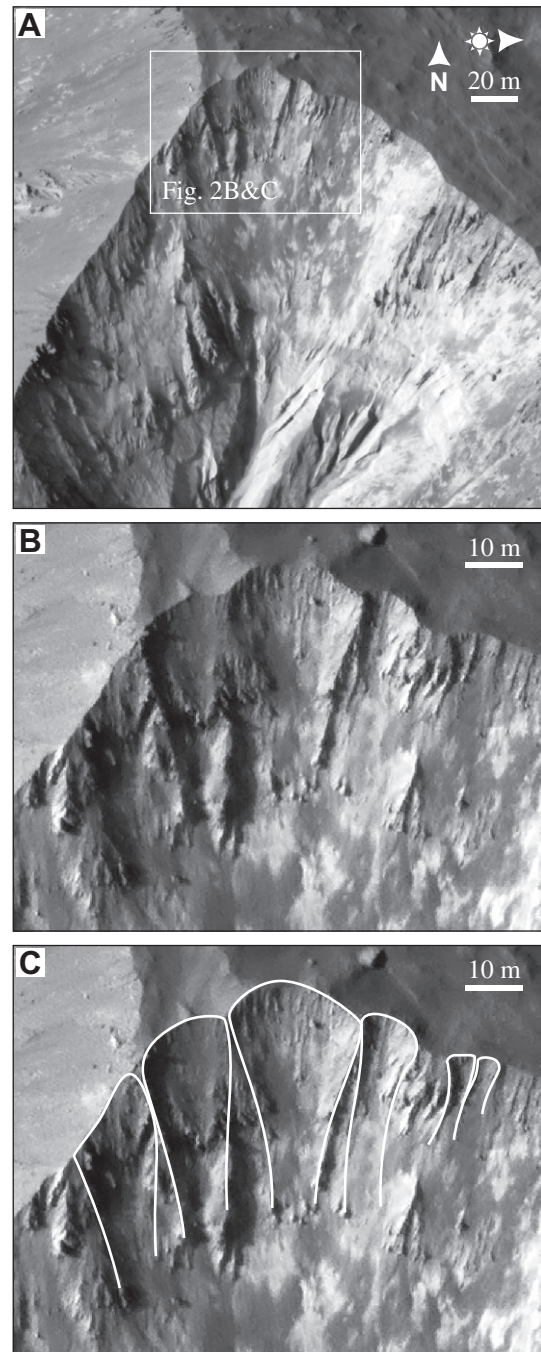

Fig. 2. (A) Well-defined scalloped depressions in the upper slopes of an alcove. (B) Close-up showing that these depressions generally narrow downslope, suggestive of the typical morphology of Earth flow scars (e.g., Varnes, 1978). (C) Same image as (B) with the depression margins outlined. Image is from HiRISE PSP_004060_1440.

reproduce the geomorphology of the alcoves are considered to be likely scenarios for the growth of these alcoves.

Limit equilibrium methods (c.f., Abramson et al., 2001) are widely used to investigate the stability of slopes in volcanic rocks on Earth (e.g., Okubo, 2004; Apuani et al., 2005; Moon et al., 2005, 2009; Neuffer et al., 2006; Longpré et al., 2007) and have also been applied to slopes on Mars (Schultz, 2002; Neuffer and Schultz, 2006; Perko et al., 2006). Of particular importance to the present analysis are the previous investigations that demonstrate the applicability of limit equilibrium methods for investigating the stability and triggering mechanisms of slope failures in the alcoves of

terrestrial gullies and hollows (e.g., Hanberg and Tripp, 1990; Lee et al., 1999; Özdemir and Delikanli, 2008; Crosta, 2001; Malet et al., 2005; Brideau et al., 2006, 2007; Ulusay et al., 2007; Poisel et al., 2009; and many others). These studies show that slope stability analysis based on limit equilibrium methods is an essential tool for understanding the geologic conditions that facilitate the growth of gully alcoves on Earth.

The primary inputs to these slope stability analyses are the topography of the slope and physical properties of the rock mass that constitutes this slope. The topography of Gasa crater is characterized by constructing a DEM from HiRISE images PSP_004060_1440 and PSP_005550_1440. The DEM is created using the commercial photogrammetric software SOCET SET (BAE Systems, 2009), following a methodology outlined by Kirk et al. (2008). The HiRISE DEM is tied to the Precision Experiment Data Records from the Mars Orbiter Laser Altimeter (MOLA), which helps to preserve regional slope and the slopes of large-scale geomorphic features such as crater walls and the slopes of hollows that were sampled by MOLA. The resulting DEM is constructed at 1 m/post. The highest resolution image of the stereo pair (PSP_004060_1440) is also orthorectified with this DEM using SOCET SET. In addition to the present work, this same HiRISE DEM and orthoimage is also used in the independent studies of Lanza et al. (2010) and Kolb et al. (2010a). The HiRISE-derived topography used here offers one to two orders of magnitude finer resolution of gully slopes that was available to previous

investigations using MOLA (e.g., Heldmann and Mellon, 2004; Heldmann et al., 2007; Dickson et al., 2007) or HRSC (e.g., Reiss et al., 2009).

The precision of elevation values in the HiRISE DEM used here can be estimated based on viewing geometry and pixel scale. The image pair PSP_004060_1440 (0.255 m/pixel) and PSP_005550_1440 (0.266 m/pixel) have a 12.6° stereoscopic convergence angle. Assuming 1/5 pixel matching error and 0.266 m/pixel in the more oblique image, the vertical precision is estimated as 0.266/5/tan(12.6°) = 0.24 m (c.f., Kirk et al., 2003). Pixel matching error is influenced by signal-to-noise ratio, scene contrast and differences in illumination between images. Pattern noise can also be introduced by the automatic terrain extraction algorithm, especially in areas of low correlation. Hand editing is necessary to correct spurious topography in areas of poor correlation and change (e.g., smooth, low contrast slopes and along shadow edges).

A series of 20 topographic profiles are extracted from the HiRISE DEM along the sections shown in Figs. 1 and 3. Each of these 20 topographic profiles is used to construct a 2D model of the respective alcove slope. Material properties of the rock mass (i.e., strength and density) are then assigned to this 2D model. The material properties used in this study are listed in Table 1 and discussed below.

The strength behavior of the rock mass is prescribed using the Hoek–Brown failure criterion for fractured rock masses (Hoek and Brown, 1980; Eq. (1)).
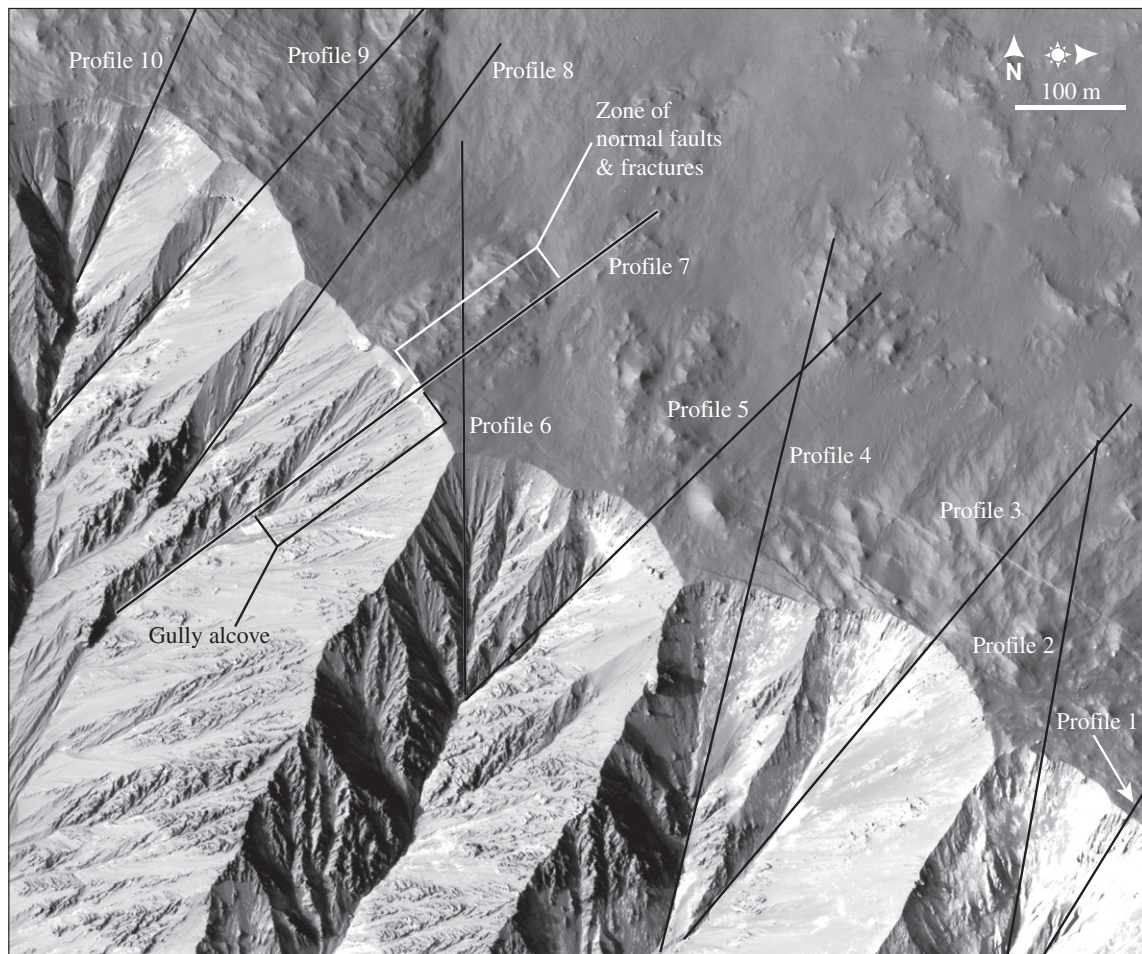

Fig. 3. Modeled profiles that are along alcoves adjacent to zones of crown fractures. Lengths of all profiles analyzed in this study were selected to transect the zone of crown fractures (where present) and extend downslope to the intersection of adjacent gullies or ridges. The location of profile 7 relative to the crown fractures and alcove rim and inner slope is highlighted to aid in the discussion of model results (c.f., Figs. 4–7). Image is from HiRISE PSP_004060_1440.

Table 1
Physical properties of the intact rock and rock mass used in this study. The melting point of H$_2$O ground ice under ambient conditions is abbreviated as *mp*. Maximum values of *RMR*, *s*, and *m* correspond to in situ basalt, while the minimum values correspond to impact breccia or colluvium.

	Frozen to dry		Melting to wet	
	Dry or cold ice (*ca.* 20–5° below *mp*)		Groundwater saturation or melting ice (<*ca.* 5° below *mp*)	
	Max	Min	Max	Min
RMR				
Minimal weathering	75	40	64	29
Highly weathered	50	10	39	0
s				
Minimal weathering	0.06218	0.00127	0.01832	0.00037
Highly weathered	0.00387	0.00005	0.00114	0.00001
m				
Minimal weathering	9.009	2.581	6.082	1.743
Highly weathered	3.689	0.884	2.490	0.619
	Mean	Std. deviation	Mean	Std. deviation
Density (kg/m^3)				
Minimal weathering	2897.5	138.3	3005.6	138.3
Highly weathered	1917.5	138.3	1983.7	138.3
UCS (intact rock, MPa)				
Minimal weathering	198	98	198	98
Highly weathered	4	2	4	2

$$\sigma_1 = \sigma_3 + \sqrt{m\sigma_c\sigma_3 + s\sigma_c^2} \qquad (1)$$

$$m = m_i \exp\left(\frac{RMR - 100}{28}\right) \qquad (2)$$

$$s = \exp\left(\frac{RMR - 100}{9}\right) \qquad (3)$$

Here, σ_c is the unconfined strength of the intact rock. Parameters *m* and *s* are dimensionless and represent the degree of fracturing and block interlocking within the rock mass. The principal stresses are σ_1 and σ_3. Values for σ_c are constrained by results of laboratory testing of terrestrial 'a'ā and pāhoehoe flows (Okubo, 2004) and flood basalts (US Department of Energy, 1988). These studies report values for unconfined compressive strength of 198 ± 98 MPa. This range of values is adopted in our stability analyses. The *m* and *s* parameters (Eqs. (2) and (3)) are calculated from *RMR* (rock mass rating) values for the rock mass and m_i, a dimensionless parameter approximating the ratio between σ_c and the tensile strength of the intact rock. Values for m_i of 18–28 are used, based on previous tests of basaltic and other igneous rock masses (Hoek et al., 1995; Schultz, 1995). Further, *s* is equal to zero for values of *RMR* less than 25 (Hoek and Brown, 1997).

Eqs. 2 and 4 (definition of *m* and *s*) are empirical relationships constructed from back calculations of failed rock masses on Earth (Hoek and Brown, 1980), where the shape of the strength envelope (i.e., what Eq. (1) is intended to describe) and the pre-failure values of *RMR* are constrained by observations. Parameters *m* and *s* are empirical estimations of intrinsic rock mass properties – roughly, functions of the tensile and cohesive strength of the rock mass as a function of *RMR*.

RMR is a standard, dimensionless metric for measuring the strength of a fractured rock mass, which encompasses the strength of the fractures and the intact blocks of rock between them (Bieniawski, 1989). Values of *RMR* range between zero for severely weathered, saturated and brecciated rock and 100 for dry, intact crystalline rock. *RMR* is calculated as the sum of five rating elements. Three elements reflect the degree of weathering (e.g., the presence of hydrated minerals) and fracturing. The remaining two elements relate to σ_c and groundwater conditions.

Values of *RMR* are generally calculated from field measurements, which are not available for this study. Alternatively, *RMR* can be calculated from geological descriptions using the Geological Strength Index (*GSI*). Similar to *RMR*, *GSI* quantifies the degree of block interlocking and weathering within the rock mass and can be used where detailed field measurements are not possible or are impractical (Hoek, 1994; Hoek et al., 1995; Hoek and Brown, 1997). *GSI* rankings are based on two general criteria, structure and degree of weathering, and the corresponding values range from 0 to 100. A rock mass that is composed of in situ, fractured but well interlocked blocks, with unweathered fracture faces has a *GSI* value of 65–100. An unweathered granitic pluton with minimal fractures is an example of this type of a rock condition. A disintegrated, heavily altered and poorly interlocked rock mass has a *GSI* value of between 0 and 30. This type of rock condition is typified by a heavily weathered, non-indurated colluvium. This range of *GSI* values brackets the array of rock mass strengths as observed on Earth. An uncertainty of roughly 20% is generally assumed when estimating *GSI* values for terrestrial rock masses (e.g., Hoek and Brown, 1997). *RMR* is calculated from *GSI* as *RMR* = *GSI* + 5 for completely dry groundwater conditions. *RMR* decreases with increasing groundwater activity, with up to a 15-point reduction for a rock mass with flowing groundwater within its fractures (Bieniawski, 1989).

The use of *RMR* and *GSI* is necessary here in order to more precisely capture the frictional and cohesive strength of the rock mass. The rock mass is an integrated system of fractures and intact blocks of rock. Therefore its strength cannot be adequately represented by simple block sliding models, where the tendency for sliding (i.e., slope failure) is governed by the frictional and cohesive strength of a single plane below an intact block of rock.

To be as inclusive as possible, this study incorporates the full range of values for *GSI* that correspond to the expected rock mass conditions and weathering state. As previously discussed, inspection of HiRISE imagery suggests that the rock mass into which the alcoves are cut consists of a range of materials from fractured, in situ basalt to impact breccia or colluvium. For this study the strengths of the in situ basalt and impact breccia/colluvium end members will be considered. Thus values of *RMR* between 0 and 75 (Table 1), out of a possible *RMR* range of 0–100, are tested here.

Observations of these alcoves by the Compact Reconnaissance Imaging Spectrometer for Mars (CRISM) show no strong evidence

Table 2
Summary of prescribed model conditions and numerical predictions for the (a) frozen to dry over melting to wet model scenarios and (b) melting to wet over frozen to dry model scenarios. The frozen to dry groundwater condition is abbreviated as 'dry', and melting to wet is abbreviated as 'wet'. Minimally weathered in situ basalt is abbreviated as a 'strong' rock mass condition, and a heavily weathered colluvium is abbreviated as 'weak'. Numerical entries are the mean values of all modeled profiles followed by the standard deviations in parentheses. Factor of Safety (FS) is calculated using the Bishop Simplified method. Values of horizontal ground acceleration (HGA) are measured with g_{Mars} equal to 3.729 m s^{-2}. Detailed model results for individual profiles are given in Appendix A.

Surface layer thickness	Rock mass strength	Crown fractures present?	Mean Probability of Failure (%)		Mean minimum Factor of Safety		Minimum HGA for Factor of Safety = 1 (gmars)
			Static	Dynamic	Static	Dynamic	Dynamic
(a)							
1 m	Strong	Yes	0.0 [0.0]	3.2 [1.5]	3.9 [0.6]	0.1 [0.0]	0.8 [0.1]
10 m	Strong	Yes	0.0 [0.0]	0.9 [0.8]	4.9 [0.8]	0.4 [0.3]	1.1 [0.2]
100 m	Strong	Yes	0.0 [0.0]	0.3 [0.2]	5.9 [0.7]	0.7 [0.3]	1.2 [0.3]
All dry	Strong	Yes	0.0 [0.0]	0.3 [0.2]	5.9 [0.7]	0.7 [0.3]	1.2 [0.2]
1 m	Weak	Yes	0.0 [0.0]	27.7 [8.2]	2.8 [0.6]	0.0 [0.0]	0.6 [0.1]
10 m	Weak	Yes	0.0 [0.0]	20.3 [8.7]	3.2 [0.5]	0.1 [0.1]	0.7 [0.1]
100 m	Weak	Yes	0.0 [0.0]	3.6 [2.1]	3.5 [0.4]	0.1 [0.1]	1.0 [0.1]
All dry	Weak	Yes	0.0 [0.0]	3.4 [2.0]	3.5 [0.4]	0.1 [0.1]	1.0 [0.0]
1 m	Strong	No	0.0 [0.0]	2.2 [0.9]	4.2 [0.3]	0.1 [0.0]	0.8 [0.1]
10 m	Strong	No	0.0 [0.0]	0.4 [0.3]	5.3 [0.6]	0.7 [0.2]	1.2 [0.1]
100 m	Strong	No	0.0 [0.0]	0.2 [0.1]	6.3 [0.6]	0.8 [0.1]	1.3 [0.1]
All dry	Strong	No	0.0 [0.0]	0.2 [0.1]	6.3 [0.6]	0.8 [0.1]	1.4 [0.1]
1 m	Weak	No	0.0 [0.0]	22.1 [4.9]	2.8 [0.2]	0.0 [0.0]	0.6 [0.1]
10 m	Weak	No	0.0 [0.0]	14.5 [6.1]	3.4 [0.3]	0.0 [0.0]	0.8 [0.1]
100 m	Weak	No	0.0 [0.0]	2.0 [1.1]	3.7 [0.2]	0.1 [0.1]	1.0 [0.0]
All dry	Weak	No	0.0 [0.0]	2.1 [1.1]	3.7 [0.2]	0.1 [0.1]	1.0 [0.0]
(b)							
1 m	Strong	Yes	0.0 [0.0]	0.2 [0.1]	6.0 [0.8]	0.3 [0.1]	1.1 [0.1]
10 m	Strong	Yes	0.0 [0.0]	1.7 [0.4]	3.4 [0.9]	0.1 [0.0]	0.7 [0.1]
100 m	Strong	Yes	0.0 [0.0]	5.9 [2.3]	3.1 [0.8]	0.0 [0.0]	0.6 [0.1]
All wet	Strong	Yes	0.0 [0.0]	6.0 [2.3]	3.0 [0.7]	0.0 [0.0]	0.7 [0.1]
1 m	Weak	Yes	0.0 [0.0]	2.8 [1.2]	3.4 [0.7]	0.1 [0.0]	0.9 [0.1]
10 m	Weak	Yes	0.0 [0.0]	13.5 [3.1]	2.4 [0.7]	0.1 [0.0]	0.4 [0.1]
100 m	Weak	Yes	0.0 [0.0]	43 [9.4]	2.1 [0.6]	0.0 [0.0]	0.4 [0.1]
All wet	Weak	Yes	0.0 [0.0]	43.3 [9.4]	2.1 [0.5]	0.0 [0.0]	0.4 [0.1]
1 m	Strong	No	0.0 [0.0]	0.1 [0.1]	6.3 [0.6]	0.3 [0.2]	1.2 [0.2]
10 m	Strong	No	0.0 [0.0]	1.7 [0.2]	4.0 [0.3]	0.1 [0.0]	0.7 [0.0]
100 m	Strong	No	0.0 [0.0]	4.4 [1.2]	3.5 [0.2]	0.0 [0.0]	0.7 [0.1]
All wet	Strong	No	0.0 [0.0]	4.4 [1.3]	3.4 [0.2]	0.0 [0.0]	0.7 [0.1]
1 m	Weak	No	0.0 [0.0]	1.7 [0.5]	3.7 [0.2]	0.1 [0.0]	0.8 [0.1]
10 m	Weak	No	0.0 [0.0]	12.2 [1.9]	2.8 [0.2]	0.1 [0.0]	0.5 [0.1]
100 m	Weak	No	0.0 [0.0]	38.8 [6.3]	2.4 [0.1]	0.0 [0.0]	0.5 [0.0]
All wet	Weak	No	0.0 [0.0]	38.9 [6.4]	2.4 [0.1]	0.0 [0.0]	0.5 [0.1]

of aqueous alteration of the rock mass exposed along the alcove walls. Even though some alteration may be expected in the rim of this crater, a signature of hydrated minerals cannot be isolated here at the scale of CRISM (roughly 18 m/pixel). This conclusion is based on examination of spectral summary products (Pelkey et al., 2007) and spectral analyses of CRISM observation FRT 00006220. HiRISE color images indicate poor bedrock exposures in the crater rim and wall, which are apparently obscured by the smooth-lying, smaller-grained deposits (Fig. S1). Thus the spectral signature of hydrated minerals within the bedrock could be concealed. Therefore the behaviors of the in situ basalt and colluvium are expanded to incorporate the range of expected strengths under both minimal and pervasive weathering conditions.

In constructing the slope stability models, the lowest (weakest) GSI values are constrained by the strength of heavily weathered, breccia/colluvium, and the highest (strongest) values reflect the strength of minimally weathered, in situ basalt with typical cooling fractures. Following GSI guidelines (e.g., Hoek and Brown, 1997), the breccia/colluvium is envisaged as a disintegrated, poorly interlocked, heavily broken rock mass with a mixture of sub-meter angular clasts. The in situ basalt is a minimally disturbed rock mass with angular, interlocked blocks. Fracture surfaces for both rock mass conditions are assumed to vary between rough and non-weathered to smooth and highly weathered. Values of GSI are assigned based on these general descriptions using a correlation chart provided by Hoek and Brown (1997) and converted to RMR (Table 1).

Table 1 lists the material properties used in the stability models. The unconfined compressive strength (UCS) of heavily weathered basalt is assumed to be 2% of the strength of non-weathered basalt (after Gupta and Rao (2000)). The density of heavily weathered basalt is prescribed as 66% of the weight of non-weathered basalt (Gupta and Rao, 2000). Density is based on the average martian southern highlands (McKenzie et al., 2002; Turcotte et al., 2002; McGovern et al., 2004) and assumes 10% H_2O (by volume) for water- or ice-saturated conditions.

The presence of interstitial H_2O ice can significantly affect the strength of a fractured rock mass. Sufficiently cold H_2O ice (ca. >20 °C below the melting point for a given pressure, salinity, etc.) can increase a rock mass' RMR by up to ca. 20% over its completely dry value (RMR$_{dry}$) (e.g., Haines and Terbrugge, 1991; Davies et al., 2000; 2001; Laubscher and Jakubec, 2001). This overall strengthening applies to rock masses in environments lacking cyclic ice wedging (e.g., Walder and Hallet, 1985; Matsuoka, 1990), which has a destabilizing effect, especially in unconfined areas (e.g., at the surface), and increases the tendency for slope failure (e.g., Matsuoka, 2007; Sandersen et al., 1996).

Increasing ground temperatures can induce significant weakening of an ice-filled rock mass before the melting point of the H_2O ice is reached (Davies et al., 2001; Ladanyi, 2006). The strength of a warming (but still frozen) ice-filled rock mass will eventually fall to the same magnitude as its RMR$_{dry}$ value. Once the ice warms to within a few degrees (ca. <5 °C) below its ambient melting point,

Table 3
Comparison of model predictions to observations for prescribed slope conditions. The frozen to dry groundwater condition is abbreviated as 'dry', and melting to wet is abbreviated as 'wet'. Minimally weathered in situ basalt is abbreviated as a 'strong' rock mass condition, and a heavily weathered colluvium is abbreviated as 'weak'. Positive correlations are indicated with Y's. Marginal designations (*m*) for crown fracture correlation means that some, but not all, of the weakest failure surfaces intersect at the top of the slope in the same location where crown fractures are observed.

Layer configuration	Loading condition	Rock mass condition	Surface layer thickness	Failure surfaces with FS < 2	Crown fracture correlation	Shallow failure surfaces	Quasi- planar failure surfaces	Best fit
Dry over wet	Static	Strong	1 m		Y			
Dry over wet	Static	Strong	10 m		Y			
Dry over wet	Static	Strong	100 m		Y			
All dry	Static	Strong	Homogeneous		Y			
Dry over wet	Static	Weak	1 m		Y			
Dry over wet	Static	Weak	10 m		Y			
Dry over wet	Static	Weak	100 m		Y			
All dry	Static	Weak	Homogeneous		Y			
Dry over wet	Dynamic	Strong	1 m	Y	*m*		Y	
Dry over wet	Dynamic	Strong	10 m	Y	Y	Y	Y	Y
Dry over wet	Dynamic	Strong	100 m	Y	Y	Y	Y	Y
All dry	Dynamic	Strong	Homogeneous	Y	Y	Y	Y	Y
Dry over wet	Dynamic	Weak	1 m	Y	*m*		Y	
Dry over wet	Dynamic	Weak	10 m	Y	*m*		Y	
Dry over wet	Dynamic	Weak	100 m	Y	Y	Y	Y	Y
All dry	Dynamic	Weak	Homogeneous	Y	Y	Y	Y	Y
Wet over dry	Static	Strong	1 m		Y			
Wet over dry	Static	Strong	10 m	Y		Y	Y	
Wet over dry	Static	Strong	100 m	Y		Y	Y	
All wet	Static	Strong	Homogeneous	Y		Y	Y	
Wet over dry	Static	Weak	1 m		Y			
Wet over dry	Static	Weak	10 m	Y		Y	Y	
Wet over dry	Static	Weak	100 m	Y	Y	Y	Y	Y
All wet	Static	Weak	Homogeneous	Y	Y	Y	Y	Y
Wet over dry	Dynamic	Strong	1 m	Y	Y	Y	Y	Y
Wet over dry	Dynamic	Strong	10 m	Y	Y	Y	Y	Y
Wet over dry	Dynamic	Strong	100 m	Y	Y		Y	
All wet	Dynamic	Strong	Homogeneous	Y	Y		Y	
Wet over dry	Dynamic	Weak	1 m	Y	Y	Y	Y	Y
Wet over dry	Dynamic	Weak	10 m	Y	Y	Y	Y	Y
Wet over dry	Dynamic	Weak	100 m	Y	Y		Y	
All wet	Dynamic	Weak	Homogeneous	Y	Y		Y	

the *RMR* of the rock mass can fall to 70% that of *RMR*$_{dry}$ (Davies et al., 2001). This means that the loss of strength induced by rising temperatures could induce slope failure before the H$_2$O ice warms to its melting point. This 20% reduction in *RMR* is also roughly comparable to the 15% decrease in *RMR* attendant with conditions of fully saturated groundwater (e.g., Bieniawski, 1989).

The effects of several conditions of groundwater and H$_2$O ice are tested in this study (Table 1). A rock mass that completely lacks H$_2$O ground ice or groundwater (i.e., *RMR*$_{dry}$) is assumed in one set of analyses. The rock mass strength that corresponds to this *RMR*$_{dry}$ condition is also roughly equivalent to a H$_2$O ice-filled rock mass at *ca.* 5–10 °C below the melting point of the ice. This set of equivalent states is hereafter abbreviated as the "frozen to dry" groundwater condition. Also tested in a parallel set of analyses is the condition where near-melting H$_2$O ground ice (ice < 5 °C below its melting point) completely fills the interstitial fractures of the rock mass. Recall that this range of *RMR* is also the same as the *RMR* for a rock mass that is saturated with groundwater. This pair of equivalent states is hereafter referred to as the "melting to wet" groundwater condition. The effects of CO$_2$ ice and clathrate hydrates on the stability of these alcove slopes are not investigated here, given that the influence of these materials on rock mass strength is largely unconstrained.

The effects of potential depth-varying groundwater conditions within the slope is investigated by modeling stacked layers that exhibit "melting to wet" and "frozen to dry" groundwater conditions. A simple two-layer model is assumed. The top layer is assigned a thickness of either 1 m, 10 m or 100 m, and the bottom layer fills

the remaining model space and is at a minimum 200 m thick. Scenarios of a "melting to wet" layer over a "frozen to dry" layer are tested, which simulates a melting surface layer, or percolating snow melt, above a dry rock mass or cryosphere. Scenarios of a "frozen to dry" layer over a "melting to wet" layer are also tested to investigate a dry rock mass or cryosphere overlying a water table. Scenarios assuming homogeneous groundwater conditions within the slope, i.e. no layering, are also tested.

Pore pressure within each "melting to wet" layer is calculated with respect to a water table that is prescribed to follow the top of the "melting to wet" layer. Pore pressure is not applied to any "frozen to dry" layers that underlie "melting to wet" layers. A water table is not prescribed in stability models for slopes assuming the homogeneous "frozen to dry" groundwater condition.

Stability is also assessed under both static and dynamic loading conditions. Under static loading conditions, gravity and any attendant pore pressure from groundwater are the only external forces acting to drive slope failure. In the dynamic loading analyses, a pseudostatic horizontal ground acceleration (HGA) acting in the out-of-slope direction is prescribed. Such loading conditions could be induced by seismic sources such as fault slip and impact cratering. Magnitudes of HGA between 0.1g_{Mars} and 1.9g_{Mars}, assuming a uniform probability distribution, are tested in all dynamic loading models. In this paper, HGA is discussed in terms of g_{Mars}, which is equal to the gravitational acceleration for Mars (3.72 m s^{-2}).

Stability analyses are constructed and processed using the commercial software Slide (Rocscience, 2009). These analyses are devised to find the least stable failure surfaces for each topographic

profile over the range of possible rock mass properties. This is accomplished through a set of probabilistic analyses, which are based on results of a structured series of deterministic analyses. A probabilistic stability analysis is selected to account for the uncertainty in rock mass properties and unknown locations of failure surfaces.

For each model run a specific combination of conditions (wet or dry, weathered or non-weathered, in situ or colluvium, etc.) are prescribed. Values for the prescribed rock mass properties m, s, density, UCS are assumed to follow a Gaussian distribution, as is common in geotechnical analyses. Specific values are then selected from these distributions using the Latin hypercube sampling method and assigned to the model. Latin hypercube sampling provides a more uniform sampling of the probable material properties than simply prescribing mean or end member properties or by random sampling. The driving and resisting stresses in these stability models are derived from the lithostatic and seismic body forces attendant with these material properties under martian gravitational acceleration. The stability models do not rely on far-field stresses acting on the model boundaries to drive slope failure.

Once an initial range of rock mass properties are assigned, the software generates a slip surface, and the stability of this surface is calculated using two-dimensional limit equilibrium methods. Once this initial calculation is complete, a different slip surface is

then generated and its stability is calculated. This process is systematically conducted for a total of 4500 slip surfaces distributed throughout the model space using the same initial set of rock mass properties. The software attempts to find the least stable failure surface geometry in each model by defining the locations of slip surfaces based on the least stable surface geometries found in the preceding calculations.

Once the initial 4500 slip surfaces are analyzed, the software selects a different range of rock mass properties, and a second set of stability analyses is conducted through another 4500 software-generated slip surfaces. A total of 2000 sets of 4500 slip surfaces are analyzed in this way, resulting in the stability of a total of 9×10^6 potential failure surfaces analyzed in each scenario.

The stability of each failure surface is measured using the Factor of Safety (FS) metric. FS is the ratio of the stresses acting to resist failure to the stresses acting to drive failure. Resisting stresses include friction and cohesion between intact blocks of rock, and driving stresses include weight of the overburden, pore pressure, and seismicity. The rock mass is predicted to be stable against failure when FS is much greater than 1; this indicates that the sum of the stresses acting to drive failure is much less than the stresses driving failure. The slope is near failure when FS is equal to 1 or slightly larger, and the slope is predicted to fail when FS is less than 1. The Factor of Safety for each scenario is calculated using both the
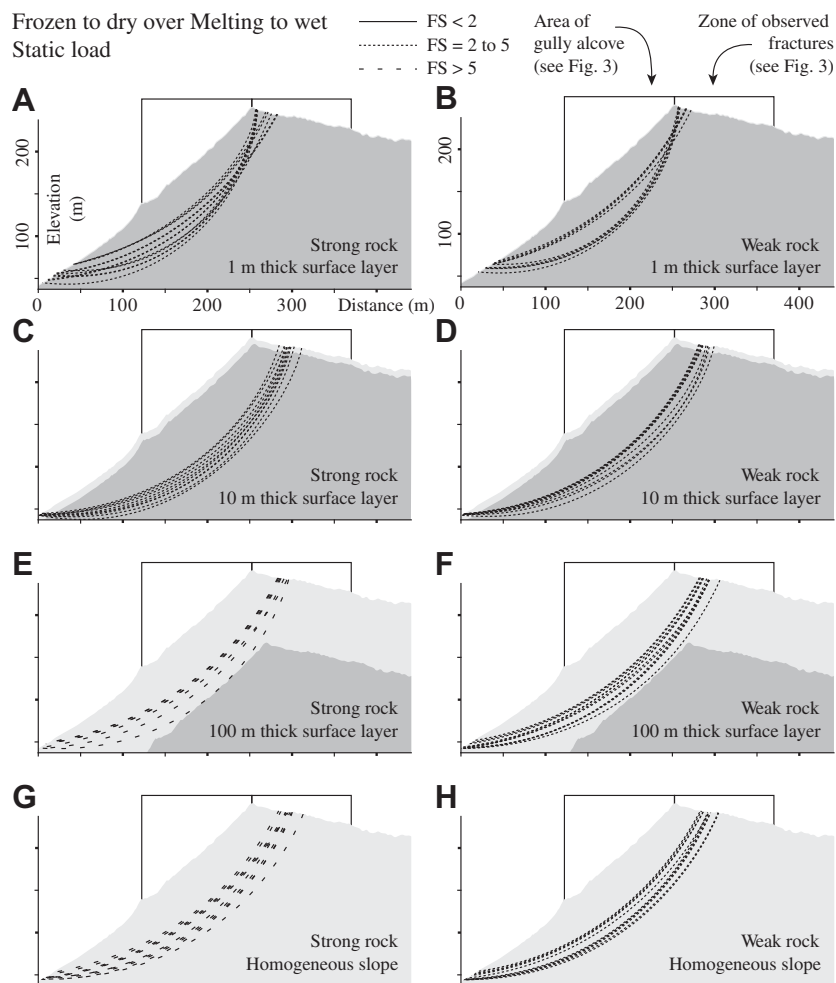

Fig. 4. Predicted failure surfaces for the model scenario of a frozen to dry over melting to wet layer configuration and static loading. Topography, location of crown fractures, and predicted failure surfaces from profile 7 are shown as a representative example. Only failure surfaces with the 10 lowest predicted values of FS_{min} (i.e., the 10 weakest surfaces) are plotted for clarity.
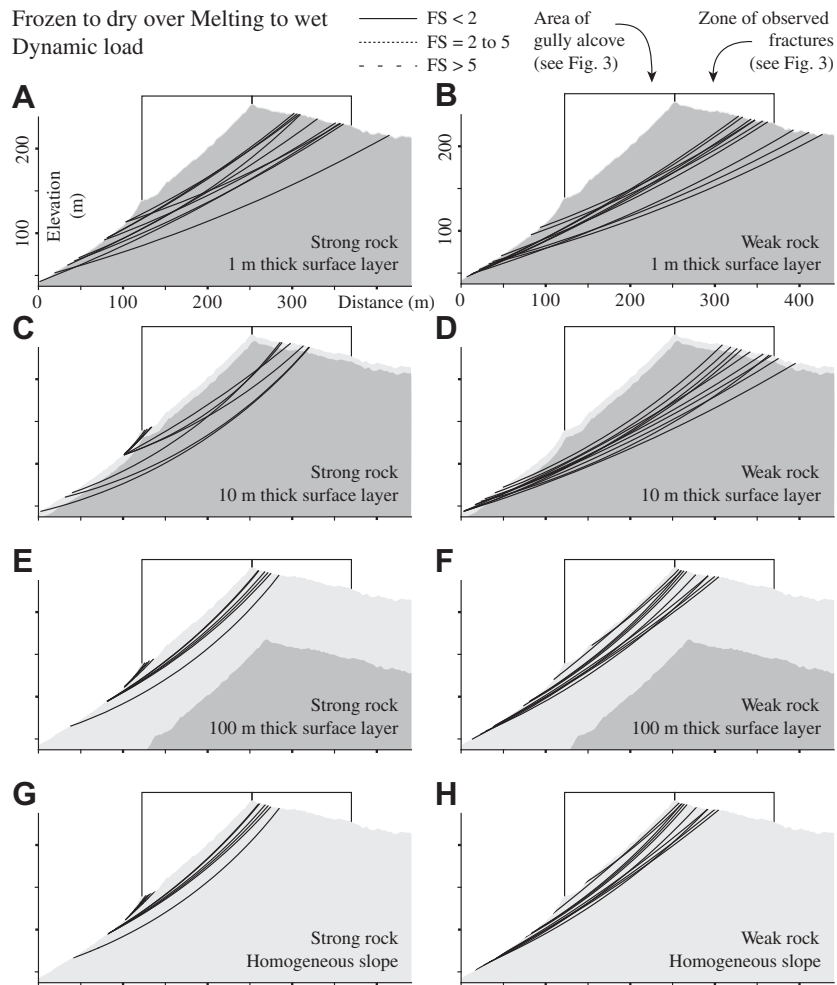
Fig. 5. Predicted failure surfaces for the model scenario of a frozen to dry over melting to wet layer configuration and dynamic loading. Results from profile 7 are shown as an example, and only failure surfaces with the 10 lowest predicted values of FS_{min} are plotted for clarity.

Bishop Simplified (Bishop, 1955) and Janbu Simplified (Janbu, 1954) limit equilibrium methods. Both methods are found to result in comparable values for FS in all cases tested here. Subsequent discussions of the model predictions will refer to values calculated using the Bishop method.

The specific number of analysis sets used here (2000) is chosen based on preliminary trial runs. Plots of mean FS versus number of sets analyzed are used to characterize the convergence of FS in the trial runs. These tests reveal that the analyses converge to within ±1 FS inside of 2000 sets (assuming 4500 slip surfaces analyzed per set). Analysis of larger numbers of sets generally do not result in a convergence to within less than ±1 FS and thus do not merit the requisite increase in processing time.

In summary, the stability of the alcove bedrock is analyzed under end member combinations of (1) "frozen to dry" or "melting to wet" groundwater conditions, (2) static or dynamic loading, (3) minimal or pervasive weathering, and (4) in situ basalt or colluvium. The best-constrained geologic condition in these analyses is the topography of the alcoves. Analyses are conducted using topographic profiles from 10 slopes within alcoves that are adjacent to crown fractures and ten slopes within alcoves that are not adjacent to crown fractures (Figs. 1 and 3). The tested combinations of conditions results in a somewhat complex matrix of results, with each topographic profile being analyzed under 32 different scenarios.

4. Results

Summaries of results from the slope stability analyses are given in Tables 2 and 3, and a comprehensive listing of all results is provided in Appendix A. In the following discussion, the predicted stability of alcove slopes is discussed in terms of the minimum FS (FS_{min}) for specific slopes and the mean minimum FS ($\overline{FS}_{min}$) of all slopes modeled under a given scenario. Model results from profile 7 are used to illustrate key points. While the potential failure surfaces for profile 7 exhibit some of the lowest predicted values of FS found in this study, profile 7 is a useful example of the overall results because the geometries of the potential failure surfaces, and the relative magnitudes of FS, are representative of results obtained from the other modeled slopes.

For the purpose of this analysis, slopes with a FS greater than 2 are considered to be stable against failure. Slopes with a FS of between 1 and 2 are considered to be near failure, and a FS of less than 1 implies incipient slope failure.

The clustering of the downslope ends of the failure surfaces in some scenarios (e.g., Fig. 4) is a result of the fact that failure surfaces that have a larger radius of curvature and greater overall area are less stable than surfaces with smaller areas and radii of curvature, assuming that all other boundary conditions are the same. Potential failure surfaces that are entirely within the existing gully alcove have predicted values of $\overline{FS}_{min}$ that are greater than (but
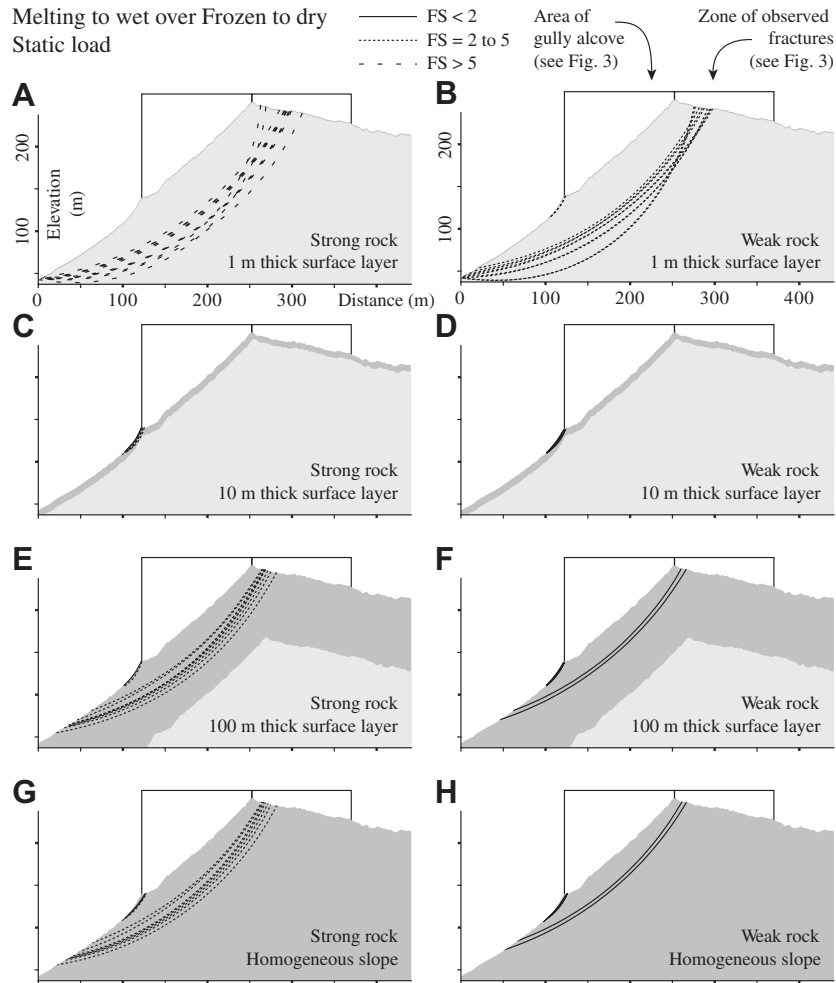
Fig. 6. Predicted failure surfaces for the model scenario of a melting to wet over frozen to dry layer configuration and static loading. Results from profile 7 are shown as an example, and only failure surfaces with the 10 lowest predicted values of FS_{min} are plotted for clarity.

within the same magnitude of) those surfaces that extend beyond the alcoves.

4.1. "Frozen to dry" over "Melting to wet"

4.1.1. Stability under static loading

Stability models of a frozen to dry layer above a melting to wet layer, i.e., water table-dependent scenarios, and under static loading, predict that all tested alcoves would be stable against slope failure (Table 2a, Fig. 4). Slopes composed of minimally weathered, in situ basalt have $\overline{FS}_{min}$ between 3.9 ± 0.6 and 6.3 ± 0.6. If the rock mass consists of highly weathered colluvium, the $\overline{FS}_{min}$ of these slopes decreases to a range of 2.8 ± 0.2 to 3.7 ± 0.2. The geometries of these failure surfaces (subtended area or radius of curvature) show no appreciable difference in strong rock versus weak rock.

For either rock mass condition, $\overline{FS}_{min}$ is predicted to consistently increase with increasing thickness of the surficial, frozen to dry, layer. That is, the alcoves are less prone to failure with increasing depth to the water table. The predicted stability of models assuming a 100 m thick frozen to dry surface layer is identical to the stability of slopes that have a homogeneous frozen to dry condition. This is due to the fact that all of the weakest surfaces in the homogeneous slope models achieve maximum depths of less than 100 m below the surface. Thus a reduction in stability due to the presence of a water table is predicted to occur if that water table is at less than 100 m below the ground surface.

A look at the geometries of the weakest failure surfaces reveals that they intersect the melting to wet layer if the water table is at less than 100 m depth. If the water table is deeper than 100 m, then the weakest failure surfaces reside entirely within the stronger frozen to dry layer. The more melting to wet area that is subtended by the failure surface, the weaker that failure surface is predicted to be (compare Fig. 4C and E). Therefore the potential for slope failure is predicted to increase with decreasing water table depth below a frozen to dry surface layer. These weakest failure surfaces show no appreciable change in geometry with increasing water table depth.

4.1.2. Stability under dynamic loading

Dynamic loading of a frozen to dry layer above a melting to wet layer is predicted to cause $\overline{FS}_{min}$ to fall below 1, implying slope failure (Table 2a, Fig. 5). Although $\overline{FS}_{min}$ is below 1 under the range of applied HGA (0.1–1.9g_{Mars}), increasing thickness of the surficial frozen to dry layer is predicted to somewhat reduce this slope instability. $\overline{FS}_{min}$ is predicted to be between zero and 0.1 ± 0 for a 1 m thick frozen to dry surface layer. $\overline{FS}_{min}$ for a 100 m thick frozen to dry surface layer, or a homogeneous frozen to dry slope, is predicted to be between 0.1 ± 0 and 0.8 ± 0.1. In all scenarios, the stability of a 100 m thick frozen to dry layer is predicted to be comparable to the stability of a homogeneous frozen to dry slope.

For the range of tested slope scenarios, values for $\overline{FS}_{min}$ of 1 are predicted when a HGA of at least 0.6 ± 0.1g_{Mars} to 1.4 ± 0.1g_{Mars}
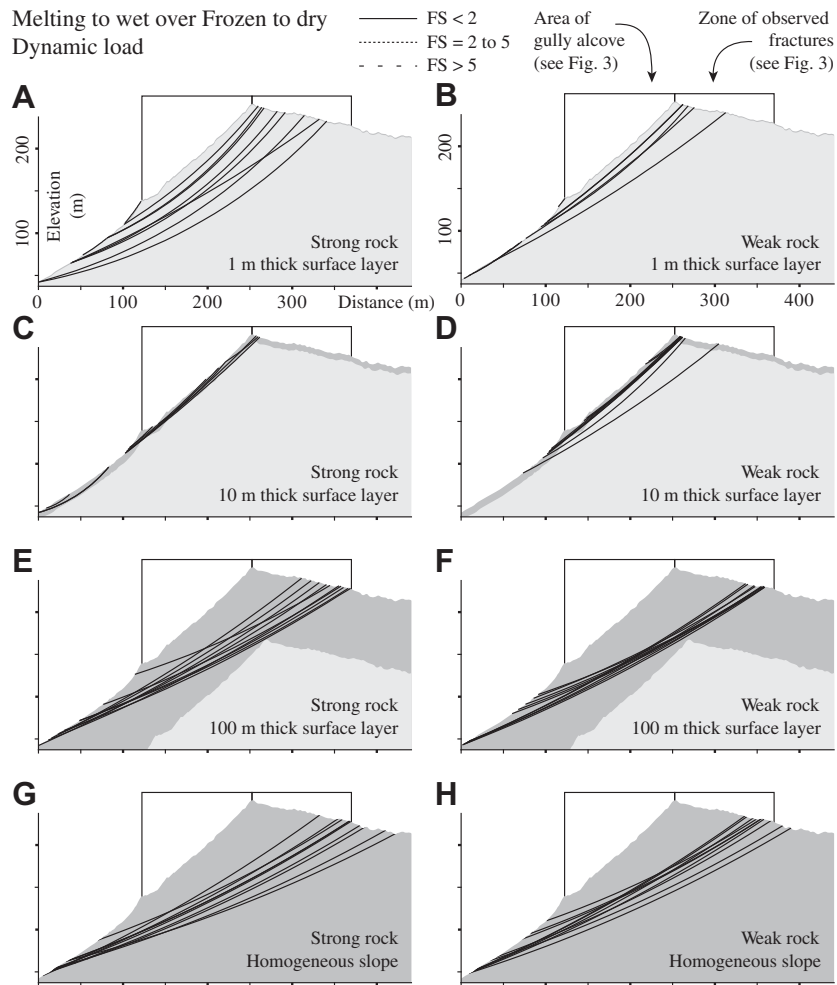
Fig. 7. Predicted failure surfaces for the model scenario of a melting to wet over frozen to dry layer configuration and dynamic loading. Results from profile 7 are shown as an example, and only failure surfaces with the 10 lowest predicted values of FS_{min} are plotted for clarity.

are applied (Table 2a). The requisite minimum magnitude of HGA for $\overline{FS}_{min} = 1$ is greatest with the thickest surficial frozen to dry layer. Similar to the static loading scenarios, this means that the alcoves are less prone to failure under dynamic loading with increasing depth to the water table. The minimum failure-inducing magnitude of HGA for a 100 m thick frozen to dry surface layer is comparable to that of a slope that is entirely frozen to dry. The magnitude of HGA required to cause failure of a rock mass consisting of heavily weathered colluvium is comparable to roughly 25% less than that of a minimally weathered, in situ basalt. As noted in the preceding discussion of the static loading scenarios, geometries of failure surfaces under dynamic loading show no appreciable difference in either strong rock versus weak rock, or with increasing water table depth.

4.2. "Melting to wet" over "Frozen to dry"

4.2.1. Stability under static loading

Stability models of a melting to wet layer above a frozen to dry layer, i.e., melting near-surface ground ice or snowmelt scenarios, and under static loading, predict that the alcoves would be either stable against slope failure or near a state of slope instability (Table 2b, Fig. 6). Slopes composed of minimally weathered, in situ basalt have $\overline{FS}_{min}$ between 3.0 ± 0.7 and 6.3 ± 0.6. If the rock mass consists of highly weathered colluvium, the $\overline{FS}_{min}$ of these

slopes decreases to a range of 2.1 ± 0.5 and 3.7 ± 0.3. The geometries of these failure surfaces show no appreciable difference in strong rock versus weak rock.

Values of $\overline{FS}_{min}$ are predicted to consistently decrease with increasing thickness of the top, melting to wet, layer. The weakest failure surfaces occur entirely within the surficial melting to wet layer. A thicker melting to wet surface layer results in deeper-cutting failure surfaces (compare Fig. 6C and E). The predicted stability of models assuming a 100 m thick melting to wet surface layer is effectively the same as the stability of slopes that have a homogeneous melting to wet condition.

Models of the 1 m thick surficial melting to wet layer predict that this relatively thin surface layer has a comparable stability to the subjacent frozen to dry layer (Fig. 6A and B). This means that a 1 m thick surficial melting to wet layer would not necessarily lead to slope failure. The surficial melting to wet layer needs to be thicker than 1 m in order to induce failure (e.g., Fig. 6C–F). This is a logical finding considering that while a 1 m thick melting to wet layer may be weaker than the subjacent frozen to dry layer, that 1 m thick layer possesses less weight, and thus less driving stress, than a thicker melting to wet surface layer. Therefore these alcoves are predicted to be more prone to failure with increasing thickness of a surficial melting to wet layer beyond a few meters. Increasing thickness of a surficial melting to wet layer would also increase the aerial extent of these failures (compare Fig. 6D and F).
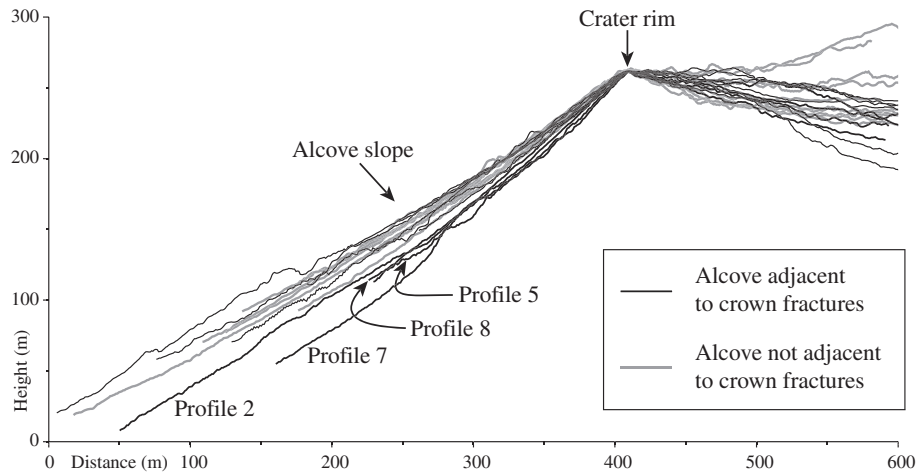
Fig. 8. Topographic profiles of all slopes analyzed in this study. Profiles are centered about the crater rim to aid in their comparison. Modeled profiles have a well-defined crater rim and alcove slopes that are slightly concave upward. The four profiles with the lowest predicted FS_{min} (2, 5, 7 and 8) have the steepest alcove slopes of all modeled profiles and transect alcoves that are adjacent to crown fractures. The dip of slopes are comparable for other, more stable, alcoves that either are or are not adjacent to crown fractures.

4.2.2. Stability under dynamic loading

Dynamic loading of a melting to wet layer above a frozen to dry layer is predicted to cause $\overline{FS}_{min}$ to be at or near zero, essentially guaranteeing slope failure (Table 2b, Fig. 7). Predicted values of $\overline{FS}_{min}$ are lowest (zero) for either a 100 m thick melting to wet surficial layer or a homogeneous melting to wet slope. $\overline{FS}_{min}$ increases slightly up to 0.3 ± 0.12 for a 1 m thick melting to wet layer. This increase in $\overline{FS}_{min}$ with decreasing thickness of the surficial melting to wet layer can again be attributed to the fact that a thinner weak layer would possess less driving stress (overburden weight) than a thicker layer.

Slope failure is favored for surfaces that lie entirely within the surficial melting to wet layer (compare Fig. 7C and E). Thus a thicker surficial melting to wet layer would also result in more aerially-extensive slope failures.

For the range of tested slope scenarios, values for $\overline{FS}_{min}$ of 1 are predicted when a HGA of at least 0.4 ± 0.1g_{Mars} to 1.1 ± 0.2g_{Mars} are applied (Table 2b). The minimum magnitude of HGA required for $\overline{FS}_{min} = 1$ increases with decreasing thickness of the surficial melting to wet layer. This is similar to the static loading scenarios in that the alcoves are predicted to be more prone to failure under dynamic loading with increasing thickness of a surficial melting to wet layer. The magnitude of HGA required to cause failure of a rock mass consisting of heavily weathered colluvium is comparable to roughly 20–30% less than that of a minimally weathered, in situ basalt.

5. Discussion

5.1. Evaluation of slope failure mechanisms

Comparison between HiRISE imagery and model results reveals intriguing correlations between predictions of slope stability and observations of slope failure (Table 3). In all scenarios, the weakest failure surfaces predicted by the stability models generally intersect with the top of the slope in or near the relative positions where crown fractures are observed (compare Fig. 3 with Figs. 4–7). A strong concurrence between predicted failure surfaces ($FS < 2$) and observed crown fracture locations is seen under conditions of (1) >ca. 10 m thick frozen to dry surface layer over melting to wet layer, with dynamic loading and weak or strong rock (Fig. 5C and E–H), (2) >100 m thick melting to wet surface layer over frozen

to dry layer, with static loading and weak rock (Fig. 6F and H), and (3) any thickness of a melting to wet surface layer over frozen to dry layer, with dynamic loading and weak or strong rock (Fig. 7).

Shallow, quasi-planar failure surfaces similar to those observed in HiRISE images (Fig. 2) are predicted under conditions of (1) >ca. 10 m thick frozen to dry surface layer over melting to wet layer, with dynamic loading and weak or strong rock (Fig. 5C and E–H), (2) >10 m thick melting to wet surface layer over frozen to dry layer, with static loading and weak or strong rock (Fig. 6C–H), and (3) a 1–10 m thick melting to wet surface layer over frozen to dry layer, with dynamic loading and weak or strong rock (Fig. 7).

Taken together, these preceding comparisons reveal several model scenarios that best fit the observed patterns of crown fractures and shallow, quasi-planar failure surfaces (Table 3). Observations can be reproduced by a >ca. 10 m thick frozen to dry surface layer overlying a melting to wet layer, with dynamic loading. Observations can also be reproduced by a >100 m thick melting to wet surface layer over frozen to dry layer, with static loading and weak rock. This surficial melting to wet layer could also be 1–10 m thick, in weak or strong rock, and still reproduce observations if dynamic loads were applied. These scenarios are therefore considered to represent the most likely conditions under which slope failure could contribute to the growth of gully alcoves in Gasa crater.

5.2. Implications of crown fractures

Another notable correlation is that slopes with the lowest predicted values of FS_{min} are generally located within alcoves that are also adjacent crown fractures (Table 2). The slopes with the four lowest predicted FS_{min} lie along profiles 2, 5, 7, and 8 (Figs. 1 and 3). These weakest slopes all have FS_{min} of less than 2.0 under static loading conditions (Appendix A) and are all located in alcoves associated with crown fractures.

An examination of the modeled topography reveals one potential cause for some slopes being less stable than others, under otherwise identical model conditions. Fig. 8 shows topographic profiles of all slopes analyzed in this study, with all profiles centered about the crater rim. The least stable alcove slopes, corresponding to profiles 2, 5, 7, and 8, are shown here to be among the steepest. First order estimates of the dip of the alcove slope can be obtained through a linear least-squares regression of the

HiRISE-derived topography between the crater rim and the down-slope terminus of the profile. The mean overall dip of the alcove slopes along these four least-stable profiles is 37°. Slopes of other, more stable alcoves are slightly shallower. The mean dip for all remaining alcove slopes is 34°. These slopes may have achieved a relatively greater stability through past failures when these alcoves were steeper and less stable.

Thus extant crown fractures may be useful morphologic indicators of existing slope instability within gully alcoves. These fractures can be used to rapidly locate gullies in other areas that would most likely undergo near-term activity through slope failure and growth of their alcoves. Such potentially active gullies are important sites for long-term monitoring and change detection.

5.3. What does HGA really mean?

A discussion relating horizontal ground acceleration (HGA) to a measure of earthquake magnitude would seem to be desirable here, in order to provide a more familiar benchmark for understanding the magnitudes of HGA being discussed in the dynamic loading models. Given that earthquake magnitude is not a function of ground acceleration alone however (e.g., Kramer, 1996), such comparisons have limited use and could be misleading. In addition to earthquake magnitude (however this magnitude is defined), the magnitude of ground acceleration experienced at a given location is also a function of other parameters such as distance from the earthquake source, crustal strength and deformability, local topography, the orientation and magnitude of the displacement vector relative to the observer, and many others.

With the preceding, significant caveat in mind, the following example is offered. Caruso (2002) investigated seismic triggering of slope failures along the northern wall of Ophir Chasma, in Valles Marineris. Calculations by Caruso (2002) suggest that a magnitude 3.6 marsquake from a surface-breaking normal fault would result in ground accelerations of $0.07g_{Mars}$ at a distance of 10 km. Given that most of the parameters that affect ground acceleration at Gasa crater are poorly constrained, or entirely unconstrained, the utility of using the calculation of Caruso (2002) to envisage the magnitudes of HGA discussed in the seismic loading sections of this paper is tenuous at best. The most practical conclusion that can be drawn from this example, if any, is that the magnitudes of HGA implied by our stability models would probably call for close proximity (within a few kilometer) to a large (10's of kilometer long) active fault. A preliminary image analysis of the area surrounding Gasa crater has not revealed any such faults. Some faults could be buried, with negligible surface expression. Small impacts may have also triggered slope failures, in the same way that they have initiated some slope streaks (e.g., Gerstell et al., 2004; Chuang et al., 2007).

6. Summary and conclusions

As shown in Table 3, model predictions from three specific combinations of conditions are most consistent with observations and are therefore the most plausible scenarios for slope failure tested in this study. Slope failure of a >*ca.* 10 m thick frozen to dry surface layer overlying a melting to wet layer, with dynamic loading is one plausible scenario. The second plausible scenario is failure of a 1–10 m thick surficial melting to wet layer, in weak or strong rock, under dynamic loading. A third plausible scenario is failure of a >100 m thick melting to wet surface layer over frozen to dry layer, with static loading and weak rock. These scenarios are predicted to result in crown fractures forming in areas where analogous fractures are observed and result in shallow, quasi-planar failure surfaces.

The finding of three plausible but distinct scenarios for slope failure supports the idea that prevailing environmental and geologic conditions affect the triggering mechanisms and characteristics of alcove growth (e.g., Reiss et al., 2009; Kolb et al., 2010a,b). Conditions that support a melting to wet rock mass would likely be most conducive to alcove rapid growth, given that dynamic loading would not be a required trigger. Slope failures in a frozen to dry rock mass would be spread over longer periods of time, since these occurrences are dependent on dynamic loading events. The resulting morphology of gullies developing under these two complementary scenarios would thus reflect "wet" processes (e.g., debris flows) predominantly, with some modification by occasional dry slope failures. With diverse failure mechanisms such as these, the gullies and hollows in Gasa crater could have evolved over a long period of time, even as environmental conditions changed. This long span of potential activity could contribute to their youthful appearance in the present day.

This study demonstrates the value of slope stability analyses for constraining plausible geologic conditions that would either enhance or impede future alcove growth. Still, the specific findings discussed here are most applicable to the 20 specific slopes studied. Much more knowledge can be gained from analysis of other gully alcoves in Gasa crater. The slopes studied here are all from large alcoves located along the upper-most reaches of hollows. Additional analysis of the smaller gully alcoves that are further downslope, as well as incorporating three-dimensional topography, are essential to better constrain the conditions under which these will gullies develop. Work such as this can serve as a benchmark for the planet-wide surveys of alcove stability that would be necessary to develop a more comprehensive understanding of how gullies form on Mars, how they will evolve over time, and any implications thereof for the necessity and origin of related groundwater activity.

Appendix A. Supplementary material

Supplementary data associated with this article can be found, in the online version, at doi:10.1016/j.icarus.2010.09.025.

References

Abramson, L.W., Lee, T.S., Sharma, S., Boyce, G.M., 2001. Slope Stability and Stabilization Methods, second ed. John Wiley & Sons, New York. 552 p.

Apuani, T., Corazzato, C., Cancelli, A., Tibaldi, A., 2005. Stability of a collapsing volcano (Stromboli, Italy): Limit equilibrium analysis and numerical modeling. J. Volcanol. Geotherm. Res. 144, 191–210. doi:10.1016/j.jvolgeores.2004.11.028.

BAE Systems, 2009. SOCET Set. <http://www.socetset.com>.

Balme, M., Mangold, N., Baratoux, D., Costard, F., Gosselin, M., Masson, P., Pinet, P., Neukum, G., 2006. Orientation and distribution of recent gullies in the southern hemisphere of Mars: observations from High Resolution Stereo Camera/Mars Express (HRSC/MEX) and Mars Orbiter Camera/Mars Global Surveyor (MOC/MGS) data. J. Geophys. Res. 111. E05001. doi:10.1029/2005JE002607.

Bart, G.D., 2007. Comparison of small lunar landslides and martian gullies. Icarus 187, 417–421. doi:10.1016/j.icarus.2006.11.004.

Bieniawski, Z.T., 1989. Engineering Rock Mass Classifications: A Complete Manual for Engineers and Geologists in Mining, Civil, and Petroleum Engineering. Wiley-Interscience, New York. 251 p.

Bishop, A.W., 1955. The use of the slip circle in the stability analysis of slopes. Geotechnique 5, 2–17.

Brideau, M.-A., Stead, D., Couture, R., 2006. Structural and engineering geology of the East Gate Landslide, Purcell Mountains, British Columbia. Can. Eng. Geol. 84, 183–206. doi:10.1016/j.enggeo.2006.01.004.

Brideau, M.-A., Stead, D., Roots, C., Orwin, J., 2007. Geomorphology and engineering geology of a landslide in ultramafic rocks, Dawson City, Yukon. Eng. Geol. 89, 171–184. doi:10.1016/j.enggeo.2006.10.004.

Bridges, N.T., Lackner, C.N., 2006. Northern hemisphere martian gullies and mantled terrain: Implications for near-surface water migration in Mars' recent past. J. Geophys. Res. 111. E09014. doi:10.1029/2006JE002702.

Caruso, P.A., 2002. Seismic Triggering of Martian Landslides and Slope Stability for Valles Marineris, Mars. M.S. Thesis, University of Nevada, Reno, 92 pp.

Christensen, P.R., 2003. Formation of recent martian gullies through melting of extensive water-rich snow deposits. Nature 422, 45–48. doi:10.1038/nature01436.

Chuang, F.C., Beyer, R.A., McEwen, A.S., Thomson, B.J., 2007. HiRISE observations of slope streaks on Mars. Geophys. Res. Lett. 34. L20204. doi:10.1029/2007GL031111.

Conway, S.J., Balme, M.R., Towner, M.C., Murray, J.B., Okubo, C.H., Grindrod, P.M., 2010. The determination of martian gully formation processes by slope-area analysis. Geological Society of London Special Paper, in press.

Costard, F., Forget, F., Mangold, N., Peulvast, J.P., 2002. Formation of recent martian debris flows by melting of near-surface ground ice at high obliquity. Science 295, 110–113. doi:10.1126/science.1066698.

Crosta, G.B., 2001. Failure and flow development of a complex slide: The 1993 Sesa landslide. Eng. Geol. 59, 173–199. doi:10.1016/S0013-7952(00)00073-9.

Cruden, D.M., Varnes, D.J., 1996. Landslide types and processes. In: Turner, A.K., Schuster, R.L. (Eds.), Landslides: Investigation and Mitigation. Transportation Research Board Spec. Pub, vol. 247. National Research Council, Washington, DC, pp. 36–75.

Davies, M.C.R., Hamza, O., Lumsden, B.W., Harris, C., 2000. Laboratory measurement of the shear strength of ice filled rock joints. Ann. Glaciol. 31, 463–468. doi:10.3189/172756400781819897.

Davies, M.C.R., Hamza, O., Harris, C., 2001. The effect of rise in mean annual temperature on the stability of rock slopes containing ice-filled discontinuities. Permafrost Periglac. 12, 137–144. doi:10.1002/ppp.378.

Dickson, J.L., Head, J.W., Kreslavsky, M., 2007. Martian gullies in the southern mid-latitudes of Mars: Evidence for climate-controlled formation of young fluvial features based upon local and global topography. Icarus 188, 315–323. doi:10.1016/j.icarus.2006.11.020.

Diniega, S., Byrne, S., Bridges, N.T., Dundas, C.M., McEwen, A.S., 2010. Seasonality of present-day Martian dune-gully activity, Geology, in press. doi: 10.1130/G31287.1.

Dundas, C.M., McEwen, A.S., Diniega, S., Byrne, S., 2010. New and recent gully activity on Mars as seen by HiRISE. Geophys. Res. Lett. 37, L07202. doi:10.1029/2009GL041351.

Gaidos, E.J., 2001. Cryovolcanism and the recent flow of liquid water on Mars. Icarus 153, 218–223. doi:10.1006/icar.2001.6649.

Gerstell, M.F., Aharonson, O., Schorghofer, N., 2004. A distinct class of avalanche scars on Mars. Icarus 168, 122–130. doi:10.1016/j.icarus.2003.11.005.

Gilmore, M.S., Phillips, E.L., 2002. Role of aquicludes in formation of martian gullies. Geology 30, 1107–1110. doi:10.1130/0091-7613(2002)030<1107:ROAIFO>2.0.CO;2.

Grant, J.A., Irwin, R.P., Grotzinger, J.P., Milliken, R.E., Tornabene, L.L., McEwen, A.S., Weitz, C.M., Squyres, S.W., Glotch, T.D., Thomson, B.J.(, 2008. HiRISE imaging of impact megabreccia and sub-meter aqueous strata in Holden Crater, Mars. Geology 36, 195–198. doi:10.1130/G24340A.1.

Gupta, A.S., Rao, K.S., 2000. Weathering effects on the strength and deformational behaviour of crystalline rocks under uniaxial compression state. Eng. Geol. 56, 257–274. doi:10.1016/S0013-7952(99)00090-3.

Haines, A., Terbrugge, P.J., 1991. Preliminary estimation of rock slope stability using rock mass classification system. In: Proc. 7th Cong. ISRM, Aachen, pp. 887–892.

Hanberg, W.C., Tripp, G., 1990. Engineering geologic investigation of an irrigation-induced debris flow near Cordova, Rio Arriba County, New Mexico. New Mexico Bureau of Mines and Geology, Open File Report 371, 80 p.

Hartmann, W.K., 2001. Martian seeps and their relation to youthful geothermal activity. Space Sci. Rev. 96, 405–410. doi:10.1023/A:1011969927462.

Head, J.W., Marchant, D.R., Kreslavsky, M.A., 2008. Formation of gullies on Mars: Link to recent climate history and insolation microenvironments implicate surface water flow origin. Proc. Natl. Acad. Sci. 105, 13258–13263. doi:10.1073/pnas.0803760105.

Hecht, M.H., 2002. Metastability of liquid water on Mars. Icarus 156, 373–386. doi:10.1006/icar.2001.6794.

Heldmann, J.L., Mellon, M.T., 2004. Observations of martian gullies and constraints on potential formation mechanisms. Icarus 168, 285–304. doi:10.1016/j.icarus.2003.11.024.

Heldmann, J.L., Carlsson, E., Johansson, H., Mellon, M.T., Toon, O.B., 2007. Observations of martian gullies and constraints on potential formation mechanisms: II. The northern hemisphere. Icarus 188, 324–344. doi:10.1016/j.icarus.2006.12.010.

Hoek, E., 1994. Strength of rock and rock masses. Int. Soc. Rock Mech. News J. 2, 4–16.

Hoek, E., Brown, E.T., 1980. Underground Excavations in Rock. Institution of Mining and Metallurgy, London. 527 p.

Hoek, E., Brown, E.T., 1997. Practical estimates of rock mass strength. Int. J. Rock Mech. Min. Sci. 34, 1165–1186. doi:10.1016/S1365-1609(97)80069-X.

Hoek, E., Kaiser, P.K., Baldwin, W.F., 1995. Support of Underground Excavations in Hard Rock. Balkema, Rotterdam. 215 p.

Hugenholtz, C.H., 2008. Frosted granular flow: A new hypothesis for mass wasting in martian gullies. Icarus 197, 65–72. doi:10.1016/j.icarus.2008.04.010.

Janbu, N., 1954. Application of composite slip circles for stability analysis. In: Proc. Europ. Conf. Stability of Earth Slopes, Stockholm, vol. 3, pp. 43–49.

Kirk, R.L., Howington-Kraus, E., Redding, B., Galuszka, D., Hare, T.M., Archinal, B.A., Soderblom, L.A., Barrett, J.M., 2003. High-resolution topomapping of candidate MER landing sites with Mars Orbiter Camera narrow-angle images. J. Geophys. Res. 108, 8088. doi:10.1029/2003JE002131.

Kirk, R.L. et al., 2008. Ultrahigh resolution topographic mapping of Mars with MRO HiRISE stereo images: Meter-scale slopes of candidate Phoenix landing sites. J. Geophys. Res. 113. E00A24. doi:10.1029/2007JE003000.

Kolb, K.J., McEwen, A.S., Pelletier, J.D., 2010a. Investigating gully flow emplacement mechanisms using apex slopes. Icarus 208, 132–142. doi:10.1016/j.icarus.2010.01.007.

Kolb, K.J., Pelletier, J.D., McEwen, A.S., 2010b. Modeling the formation of bright slope deposits associated with gullies in Hale Crater, Mars: Implications for recent liquid water. Icarus, in press. doi:10.1016/j.icarus.2009.09.009.

Kramer, S.L., 1996. Geotechnical Earthquake Engineering. Prentice Hall, New Jersey. 563 p.

Ladanyi, B., 2006. The effect of rise in mean annual temperature on the stability of rock slopes containing ice-filled discontinuities. Can. J. Civ. Eng. 33, 719–725. doi:10.1139/L05-112.

Lanza, N.L., Meyer, G., Okubo, C., Newsom, H.E., Wiens, R.C., 2010. Evidence for debris flow and shallow subsurface flow on Mars. Icarus 205, 103–112. doi:10.1016/j.icarus.2009.04.014.

Laubscher, D.H., Jakubec, J., 2001. The MRMR rock mass classification for jointed rock masses. In: Hustrulid, W.A., Bullock, R.L. (Eds.), Underground Mining Methods: Engineering Fundamentals and International Case Studies. Society for Mining, Metallurgy, & Exploration, Colorado, pp. 475–481.

Lee, H., Locat, J., Dartnell, P., Israel, K., Wong, F., 1999. Regional variability of slope stability: Application to the Eel margin, California. Mar. Geol. 154, 305–321. doi:10.1016/S0025-3227(98)00120-0.

Levy, J.S., Head, J.W., Marchant, D.R., Dickson, J.L., Morgan, G.A., 2009. Geologically recent gully-polygon relationships on Mars: Insights from the Antarctic Dry Valleys on the roles of permafrost, microclimates, and water sources for surface flow. Icarus 201, 113–126. doi:10.1016/j.icarus.2008.12.043.

Longpré, M.-A., del Potro, R., Troll, V.R., Nicoll, G.R., 2007. Engineering geology and future stability of the El Risco landslide, NW-Gran Canaria, Spain. Bull. Eng. Geol. Env. 67, 165–172. doi:10.1007/s10064-007-0119-9.

Malet, J.-P., Laigle, D., Remaitre, A., Maquaire, O., 2005. Triggering conditions and mobility of debris flows associated to complex earthflows. Geomorphology 66, 215–235. doi:10.1016/j.geomorph.2004.09.014.

Malin, M.C., Edgett, K.S., 2000. Evidence for recent groundwater seepage and surface runoff on Mars. Science 288, 2330–2335. doi:10.1126/science.288.5475.2330.

Martel, S.J., 2004. Mechanics of landslide initiation as a shear fracture phenomenon. Mar. Geol. 203, 319–339. doi:10.1016/S0025-3227(03)00313-X.

Marzo, G.A., Davila, A.F., Tornabene, L.L., Dohm, J.M., Fairén, A.G., Gross, C., Kneissl, T., Bishop, J.L., Roush, T.L., McKay, C.P., 2010. Evidence for Hesperian impact-induced hydrothermalism on Mars. Icarus, in press. doi:10.1016/j.icarus.2010.03.013.

Matsuoka, N., 1990. Mechanisms of rock breakdown by frost action: An experimental approach. Cold Reg. Sci. Technol. 17, 253–270. doi:10.1016/S0165-232X(05)80005-9.

Matsuoka, N., 2007. Frost weathering and rockwall erosion in the southeastern Swiss Alps: Long-term (1994–2006) observations. Geomorphology 99, 353–368. doi:10.1016/j.geomorph.2007.11.013.

McEwen, A.S. et al., 2007. A closer look at water-related geologic activity on Mars. Science 317, 1706–1709. doi:10.1126/science.1143987.

McGovern, P.J. et al., 2004. Correction to Localized gravity/topography admittance and correlation spectra on Mars: Implications for regional and global evolution. J. Geophys. Res. 109, E07007. doi:10.1029/2004JE002286.

McKenzie, D., Barnett, D.N., Yuan, D.N., 2002. The relationship between Martian gravity and topography. Earth and Planetary Science Letters 195, 1–16. doi:10.1016/S0012-821X(01)00555-6.

Mellon, M.T., Phillips, R.J., 2001. Recent gullies on Mars and the source of liquid water. J. Geophys. Res. 106, 23165–23180.

Moon, V., Bradshaw, J., Smith, R., de Lange, W., 2005. Geotechnical characterisation of stratocone crater wall sequences, White Island Volcano, New Zealand. Eng. Geol. 81, 146–178. doi:10.1016/j.enggeo.2005.07.014.

Moon, V., Bradshaw, J., de Lange, W., 2009. Geomorphic development of White Island Volcano based on slope stability modeling. Eng. Geol. 104, 16–30. doi:10.1016/j.enggeo.2008.08.003.

Neuendorf, K.K.E., Kehl, J.P., Jackson, J.A., 2005. Glossary of Geology, fifth ed. American Geological Institute, Falls Church, Virginia.

Neuffer, D.P., Schultz, R.A., 2006. Mechanisms of slope failure in Valles Marineris, Mars. Q. J. Eng. Geol. Hydrogeol. 39, 227–240. doi:10.1144/1470-9236/05-042.

Neuffer, D.P., Schultz, R.A., Watters, R.J., 2006. Mechanisms of slope failure on Pyramid Mountain, a subglacial volcano in Wells Gray Provincial Park, British Columbia. Can. J. Earth Sci. 43, 147–155. doi:10.1139/E05-100.

Okubo, C.H., 2004. Rock mass strength and slope stability of the Hilina slump, Kīlauea volcano, Hawai'i. J. Volcanol. Geotherm. Res. 138, 43–76. doi:10.1016/j.jvolgeores.2004.06.006.

O'Reilly, B.M., Shannon, P.M., Readman, P.W., 2007. Shelf to slope sedimentation processes and the impact of Plio-Pleistocene glaciations in the northeast

Atlantic, west of Ireland. Mar. Geol. 238, 21–44. doi:10.1016/j.margeo.2006.12.008.

Özdemir, A., Delikanli, M., 2008. A geotechnical investigation of the retrogressive Yaka Landslide and the debris flow threatening the town of Yaka (Isparta, SW Turkey). Nat. Haz. 49, 113–136. doi:10.1007/s11069-008-9282-y.

Pelkey, S.M. et al., 2007. CRISM multispectral summary products: Parameterizing mineral diversity on Mars from reflectance. J. Geophys. Res. 112. E08S14. doi:10.1029/2006JE002831.

Pelletier, J.D., Kolb, K.J., McEwen, A.S., Kirk, R.L., 2008. Recent bright gully deposits on Mars: Wet or dry flow? Geology 36, 211–214. doi:10.1130/G24346A.1.

Perko, H.A., Nelson, J.D., Green, J.R., 2006. Mars soil mechanical properties and suitability of Mars soil stimulants. J. Aerospace Eng. 19, 169–176. doi:10.1061/(ASCE)0893-1321(2006)19:3(169).

Poisel, R., Angerer, H., Pollinger, M., Kalcher, T., Kittl, H., 2009. Mechanics and velocity of the Lärchberg–Galgenwald landslide (Austria). Eng. Geol. 109, 57–66. doi:10.1016/j.enggeo.2009.01.002.

Reiss, D., Hiesinger, H., Hauber, E., Gwinner, K., 2009. Regional differences in gully occurrence on Mars: A comparison between the Hale and Bond craters. Planet. Space Sci. 57, 958–974. doi:10.1016/j.pss.2008.09.008.

Rocscience Inc., 2009. Slide. <http://www.rocscience.com>.

Sandersen, F., Bakkehøi, S., Hestnes, E., Lied, K., 1996. The influence of meteorological factors on the initiation of debris flows, rockfalls, rockslides and rockmass stability. In: Senneset, K. (Ed.), Landslides. Balkema, Rotterdam, pp. 97–114.

Schon, S.C., Head, J.W., Fassett, C.I., 2009. Unique chronostratigraphic marker in depositional fan stratigraphy on Mars: Evidence for ca. 1.25 Ma gully activity and surficial meltwater origin. Geology 37, 207–210. doi:10.1130/G25398A.1.

Schultz, R.A., 1995. Limits on strength and deformation properties of jointed basaltic rock masses. Rock Mech. Rock Eng. 28, 1–15.

Schultz, R.A., 2002. Stability of rock slopes in Valles Marineris, Mars. Geophys. Res. Lett. 29, 1932. doi:10.1029/2002GL015728.

Shinbrot, T., Duong, N.-H., Kwan, L., Alvarez, M.M., 2004. Dry granular flows can generate surface features resembling those seen in martian gullies. Proc. Natl. Acad. Sci. 101, 8542–8546. doi:10.1073/pnas.0308251101.

Tornabene, L.L., Moersch, J.E., McSween Jr., H.Y., McEwen, A.S., Piatek, J.L., Milam, K.A., Christensen, P.R., 2006. Identification of large (2–10 km) rayed craters on Mars in THEMIS thermal infrared images: Implications for possible martian meteorite source regions. J. Geophys. Res. 111. E10006. doi:10.1029/2005JE002600.

Treiman, A.H., 2003. Geologic settings of martian gullies: Implications for their origins. J. Geophys. Res. 108, 8031. doi:10.1029/2002JE001900.

Turcotte, D.L., Shcherbakov, R., Malamud, B.D., Kucinskas, A.B., 2002. Is the Martian crust also the Martian elastic lithosphere? J. Geophys. Res. 107, 5091. doi:10.1029/2001JE001594.

Ulusay, R., Aydan, Ö., Kilic, R., 2007. Geotechnical assessment of the 2005 Kuzulu landslide (Turkey). Eng. Geol. 89, 112–128. doi:10.1016/j.enggeo.2006.09.020.

US Department of Energy, 1988. Consultation Draft, Site Characterization Plan, Reference Repository Location, Hanford Site, Washington. US Department of Energy, Washington, D.C., DOE/RW-0164, Unpaginated.

Varnes, D.J., 1978. Slope movement types and processes. In: Schuster, R.L., Krizek, R.J. (Eds.), Landslides: Analysis and Control. Transportation Research Board Spec. Pub, vol. 176. National Research Council, Washington, DC, pp. 12–33.

Walder, J.S., Hallet, B., 1985. A theoretical model of the fracture of rock during freezing. Geol. Soc. Am. Bull. 96, 336–346. doi:10.1130/0016-7606(1985)96<336:ATMOTF>2.0.CO;2.